Colloids and Surfaces A: Physicochemical and Engineering Aspects 689 (2024) 133668

Contents lists available at ScienceDirect

Colloids and Surfaces A: Physicochemical and Engineering Aspects

journal homepage: www.elsevier.com/locate/colsurfa

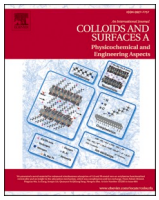

Effect of contact angle on the pressure needed for a liquid to permeate a cylindrical pore

Daniel Lippert [a], William Ducker [b], Dongjin Seo [a,*]

[a] Department of Chemical Engineering, Brigham Young University, Provo, UT 84602, USA
[b] Department of Chemical Engineering, Virginia Tech, Blacksburg, VA 24061, USA

GRAPHICAL ABSTRACT

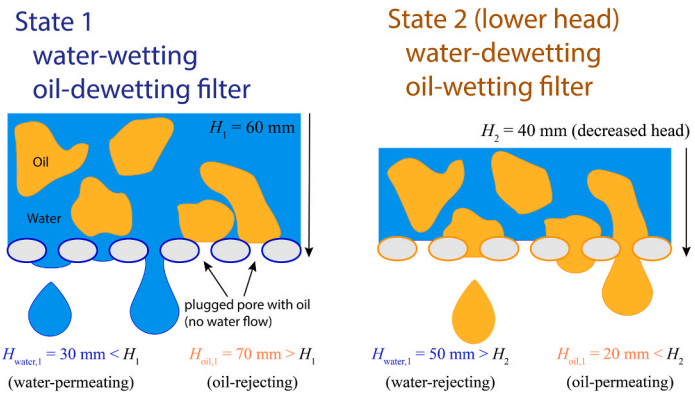

ARTICLE INFO

Keywords:
Filters
Permeation
Wettability
Separation

ABSTRACT

Effective separation of two immiscible liquids with filters requires a difference in the pressures to permeate between the two liquids, and setting the applied pressure between these two pressures. To help design such filters, we present an equation that enables the calculation of the pressure for a liquid phase to permeate through a smooth pore in the shape of a truncated cone as a function of (a) the contact angle of the liquid on the filters and (b) the angle of the pore wall. The equation was derived by considering the interfacial energy required to push a liquid meniscus from the top of the pore to the bottom, and then to exceed the maximum curvature required at the exit. This equation was tested experimentally by adding a hydrostatic head with water on the 3D-printed filters of acrylate polymer while systematically varying the pore radii and contact angle with water. Experimental results showed an increased pressure to permeate with higher contact angles while the equation predicted the opposite. We hypothesized that the reason for the disagreement was the assumption of a smooth pore. For a liquid on a rough pore wall, the curvature of the meniscus is not solely determined from the microscopic contact angle and the pore wall angle, but the liquid would adopt a lower curvature meniscus. Therefore, the developed equation was modified after reflecting the lower curvature, which showed much better agreement with the experimental results. The remaining discrepancy from the theory was attributed to the pressure fluctuation from the fluid flow occurring while adding water.

* Corresponding author.
E-mail address: dongjin.seo@byu.edu (D. Seo).

https://doi.org/10.1016/j.colsurfa.2024.133668
Received 30 December 2023; Received in revised form 18 February 2024; Accepted 8 March 2024
Available online 11 March 2024

1. Introduction

Surface wettability plays a pivotal role in determining the functionality and utility of a material. [1–5] Therefore, extensive research has been conducted on the behavior of liquids on rough or porous materials in relation to wetting transitions to achieve desired functionalities. [6–10]

Most theoretical studies on wetting transitions consider the situation where the pores are open at one end and closed at the other end. However, a large class of applications, including fabrics, filters, and membranes, deal with surfaces where the pores are open at both ends. Microfluidics also involves channels with two open ends, where fluid flow occurs and the influence of momentum and interfacial energy becomes significant in narrow channels. [11–13] One can dominate over the other depending on the size of the channel and the wettability of specific liquids on the material with which the channels are made. One of the areas in which wettability plays a critical role is liquid-liquid separation using filter and thin membranes [14–16] due to their substantially smaller lengths of channels compared to the opening areas of the pores, in contrast to microfluidic channels. While extensive research exists on flow through long, thin channels, and abundant are articles addressing the onset of flow at the gate of pores that do not concern the flow inside the pores, the studies focusing on flow through pores with their depth or length comparable to their radii are relatively scarce. This research endeavors to address this knowledge gap, aiming to deepen our understanding of how wettability affects liquid flow through such pores and ultimately enhance the utility of fabrics, filters, and thin membranes.

Our focus here is on filters and membranes that separate two immiscible liquid phases, especially oil and water. [14–16] These filters leverage the fact that liquid phases that wet the pore materials of filters and membranes (showing high wettability or low contact angle) can permeate through them without much external pressure. Simultaneously, other phases with high contact angles are retained due to the higher energy requirement when increasing the solid–liquid interfacial area, which requires an additional pressure for the liquid to permeate. If the applied pressure is set between the two pressures to permeate, separation can be achieved.

The selectivity in permeation based on wettability has motivated the development of filters with hydrophilic polymer materials due to their ease of fabrication and cost-effectiveness. Significant efforts have been directed toward altering surface properties to selectively permit the desired phases (typically water) to pass while rejecting others (usually oil). [17–21] Indeed, many studies have demonstrated high separation efficiency, even achieving near-perfect separation, by rendering their materials highly hydrophilic. [14,22–24] These studies, however, demonstrated how membranes or filters allow only the water phase to permeate from oil–water mixtures that are already well-separated by gravity, which lacks practical effectiveness for emulsified mixtures. There are also reports addressing the separation of emulsions or oil droplets in water. [14,25] Numerous techniques for this purpose have demonstrated high water throughput by rendering solids or hydrogels with which filters are made highly hydrophilic. Additionally, they exhibit anti-oil-fouling functionality by making oil adhesion less favorable to solid or hydrogel surfaces. Nevertheless, it is essential to note that, over time, oil will inevitably adhere to solid surfaces, eventually clogging the pores. [14,22–25]

Consequently, fouling remains an intrinsic problem in liquid–liquid separation techniques involving emulsified mixtures. One solution is to halt the separation process and remove the retentate that fouls the filter. However, this approach is unfavorable due to increased costs and time. An alternative remedy is to temporarily apply increased pressure, allowing the intended permeating phase to still pass through the pores. This also means the permeation of the intended retentate, thereby undermining the purpose of separation. Therefore, it becomes imperative to determine this threshold pressure, enabling decision-making regarding whether to increase pressure despite the permeation of both phases or prioritize selectivity by keeping the pressure low. While this threshold pressure can be determined through trial-and-error experiments, having predictable values becomes essential for designing large-scale processes and equipment.

Another approach to address fouling involves temporarily altering the wettability of filters *in situ*, transitioning them from being water-wetting to oil-wetting, so as to enable the fouling phase to be removed. This method is highly sought after and has seen various successful implementations. Some have achieved wettability changes by manipulating temperature [26–30], while others have employed changes in pH [31]. Additionally, there are methods involving electrochemical or electrical techniques. [32–36] While these and other instances of active wettability changes have proven effective in separating oil from water, [37] understanding the threshold pressure remains crucial for achieving high selectivity.

A switch in wettability is not sufficient for achieving high selectivity. The applied pressure (hydrostatic head) must also be adjusted, and this is where the need for a predictive equation arises. To understand this, consider a scenario where an active filter can transition from a state where its surfaces are water-wetting and oil-dewetting (State 1) to a state where it becomes oil-wetting and water-dewetting (State 2). The notion of wetting or dewetting characteristics is relative to the other phase. Water mixed with oil droplets is to be separated with this active filter. Depending on wettability, the hydraulic heads needed for each liquid phase to permeate in each state are different owing to different wettability as illustrated in Fig. 1. Presume the hydraulic head needed for water to permeate at State 1, $H_{\text{water},1}$, is 30 mm and that for oil, $H_{\text{oil},1}$, is 70 mm. When the height of liquid over the filter, H_1, is between 30 mm and 70 mm, for example, $H_1 = 60$ mm, water permeates while oil is rejected. If the wetting properties are now altered to State 2, where $H_{\text{water},2} = 50$ mm and $H_{\text{oil},2} = 20$ mm, separation can only be achieved if the head is between 50 mm and 20 mm, so the head must be reduced from the original 60 mm. While H_2 can be found with trial and error, this can be time-consuming and may cause an interruption in the separation process. Therefore, it is desirable to predict H_2 for more efficient separation operation. Hence, for both active and non-active filters, it is necessary to predict the pressure or hydraulic head required for the exclusive permeation of a single phase.

The Hagen–Poiseuille equation describes flows through and pressure differences inside a channel even in the context of small pores. However, this equation does not account for end effects where wetting occurs, which become dominants in the geometry of interest where the depth of the pore is comparable to the radius of the pore. Porosimetry, on the other hand, considers the pressure at the initiation of flow at the gate of pores. [38,39] However, this technique only accounts for the Laplace pressure at the entrance of a pore and does not describe the adhesion energy required to wet the inner wall of the pore when the depth is comparable to the radius or length.

Therefore, this article aims at the development of an equation for calculating the interfacial energy that must be overcome to enable a liquid phase to pass through a geometrically well-defined pore and detach from the exit. As a result, this equation will incorporate end effects and the interfacial energy required while liquids move inside pores. Once this equation is established, it will provide the basis for calculating the minimum pressure required for a liquid to permeate and generate a flux, denoted as "pressure to permeate". Furthermore, experimental tests were conducted to validate the developed equation. Specifically, the pressure to permeate water was measured as a function of advancing contact angles. Note that this article will not explore the effects of pore radius or liquid surface tension. However, subsequent equations, such as Eqs. (16) – (19), will demonstrate their obvious effects. In conducting these experiments, the authors prioritized practical applicability to industrialization. Accordingly, the pores were prepared using resin and 3D printing. The primary objective of this paper was to test the effect of contact angles, and the experiments were designed accordingly.

However, the effect of the pore wall angle was also included in an attempt to reconcile the data with the theory.

2. Theory

The equation for the pressure to permeate is derived for a truncated cone. This derivation is developed for pores whose radius is comparable to its height as shown in Fig. 2, and it can also be applied to pores or channels of varying depths or heights. We consider the case of (a) a thin pore of small radius such that the difference in the hydrostatic head within the pore is negligible (low Bond number, Bo) and (b) a slow flow rate such that the Hagen–Poiseuille pressure is negligible (low Capillary number, Ca). In practice, the pore radius should be less than 850 μm for water to have Bo < 0.1. We consider a pore with the shape of a truncated cone, which introduces the additional variable of the pore wall angle, α_j (Fig. 2). Note that the pore angle affects the equilibrium curvature of the meniscus. Fig. 2 illustrates how the same contact angle can lead to the opposite curvature of meniscus if the wall angle is changed. The sum of the contact angle and the wall angle for the truncated cone takes on the role of the contact angle for the straight pore. This has obvious implications for the pressure to permeate.

The critical steps in permeation are shown in Fig. 3. A liquid *i* (colored in blue) forms a contact angle θ_i on the filter material (colored in grey). The bottom opening of the pore has radius r_0, and the thickness of the filter is denoted as h_0. The position of the three-phase boundary is denoted as h measured from the bottom of the pore. The angle α_j, characterizing the angle of the wall at a specific geometry *j*, is measured from the bottom surface. For instance, $\alpha_j = 90^\circ$ indicates a cylindrical pore. Fig. 3 provides an example where $\alpha_j = 80^\circ$ but this derivation is applicable for any α_j between 0 and 180°. The notation *A* represents an interfacial area, with subscripts denoting S for solid, L for liquid, and V for vapor. The final subscript signifies the location of the three-phase boundary of the meniscus, relative to the bottom of the filter pore. Thus, the last subscript *h* denotes the meniscus at the top and 0 denotes the bottom. Four states during permeation are shown: (1) the initial placement of liquid on the top of a pore, (2) the three-phase boundary at the exit of the pore by increasing the liquid-solid interfacial area, (3) a flattened meniscus achieved after applying pressure to State (2), and (4) the growth of the droplet after achieving the minimum curvature of the interface. The transitions between states are called steps. Note that the states shown here are used for derivation and calculation purposes to compare the energy and pressure needed for each step, and not all of them are stable. As will be explained, Panel 1 A is not stable because Panel 2 A is a more preferred state. Even Panel 2 A would not be observed if the hydraulic head is high enough to make the concave meniscus bulge while the meniscus similar to that depicted in Panel 2 A can exist with a very small amount of water inside a pore.

The first step in permeation is to apply pressure to push the meniscus from the top to the bottom of the pore (Panel 1–2 in Fig. 3). When a liquid is placed on the top of a filter with pores depicted in Fig. 3, it forms a meniscus, and its shape is determined by α_j and θ_i. It then has to be pushed to the bottom of the pore. The derivation for this step closely follows that of Kaufman et al. [40] They derived the equation with a specific assumption of $r_o \gg h$, whereas our derivation does not rely on that assumption. The calculation involves determining the change in surface energy between the two stages described in Panels 1 and 2. Therefore, areas that remain constant throughout the two stages, namely the liquid-solid interfaces at the top of the filter and the solid-vapor interfaces at the bottom, are not considered.

In Panel 1, the sum of all interfacial energy, E_1, is:

$$E_1 = A_{LV,}\,\gamma_{LV} + A_{SV,h}\,\gamma_{SV} + A_{SL,h}\,\gamma_{SL}. \quad (1)$$

Likewise, in Panel 2, the sum of all interfacial energy, E_1, is:

$$E_2 = A_{LV,0}\,\gamma_{LV} + A_{SV,0}\,\gamma_{SV} + A_{SL,0}\,\gamma_{SL}. \quad (2)$$

The energy needed to push the meniscus down to the bottom is;

$$E_2 - E_1 = (A_{LV,0} - A_{LV,h})\gamma_{LV} + (A_{SV,0} - A_{SV,h})\gamma_{SV} + (A_{SL,0} - A_{SL,h})\gamma_{SL}. \quad (3)$$

$A_{SL,h} = 0$ because the wall of the pore has no contact with the liquid when the position of the meniscus is $h = h$. Likewise, $A_{SV,0} = 0$ because the wall of the pore has no contact of vapor at $h = 0$. Given that $A_{SL,h} = A_{SV,0} = 0$, and Young's equation ($\gamma_{SV} - \gamma_{SL} = \gamma_{LV}\cos\theta_i$), Eq. (3) reduces to:

$$E_2 - E_1 = \gamma_{LV}\,(A_{LV,0} - A_{LV,h} - A_{SL,0}\cos\theta_i) \quad (4)$$

Panels 1 A and 1B describe the liquid after it is placed on the top of the filter and establishes the equilibrium contact angle with the three-phase line at the pore entrance. If $\alpha_j + \theta_i < 180^\circ$, the meniscus of the liquid-vapor interface will be concave toward the liquid, and if $\alpha_j + \theta_i > 180^\circ$, it will be convex. Using the assumption that the pore radius is small (small Bo), the air–liquid interface of the meniscus is a spherical cap with area:

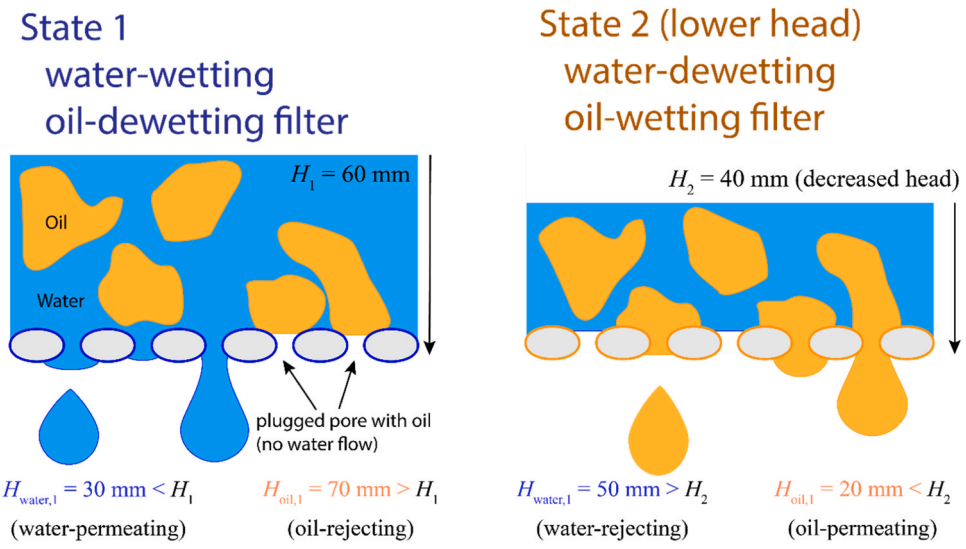

Fig. 1. Illustration of the need for predicting the right head required for each phase to permeate in an active filter that can control wettability in situ. $H_{i,j}$ is the hydraulic head needed for Species i to permeate at State j. H_1 is the hydraulic head due to the height of the mixture above the filter at the beginning of the operation, and H_2 is the head after the adjustment. All values presented here are made up for illustration purposes.

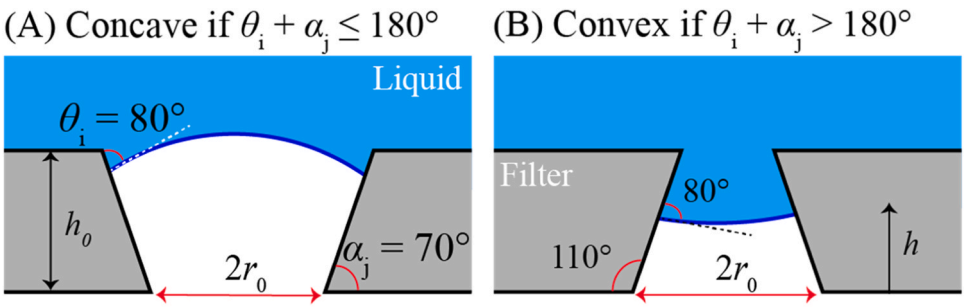

Fig. 2. Definitions of geometry used in derivation. Note that the curvature of the fluid–fluid interface depends on the contact angle, θ_i, and pore wall angle, α_j.

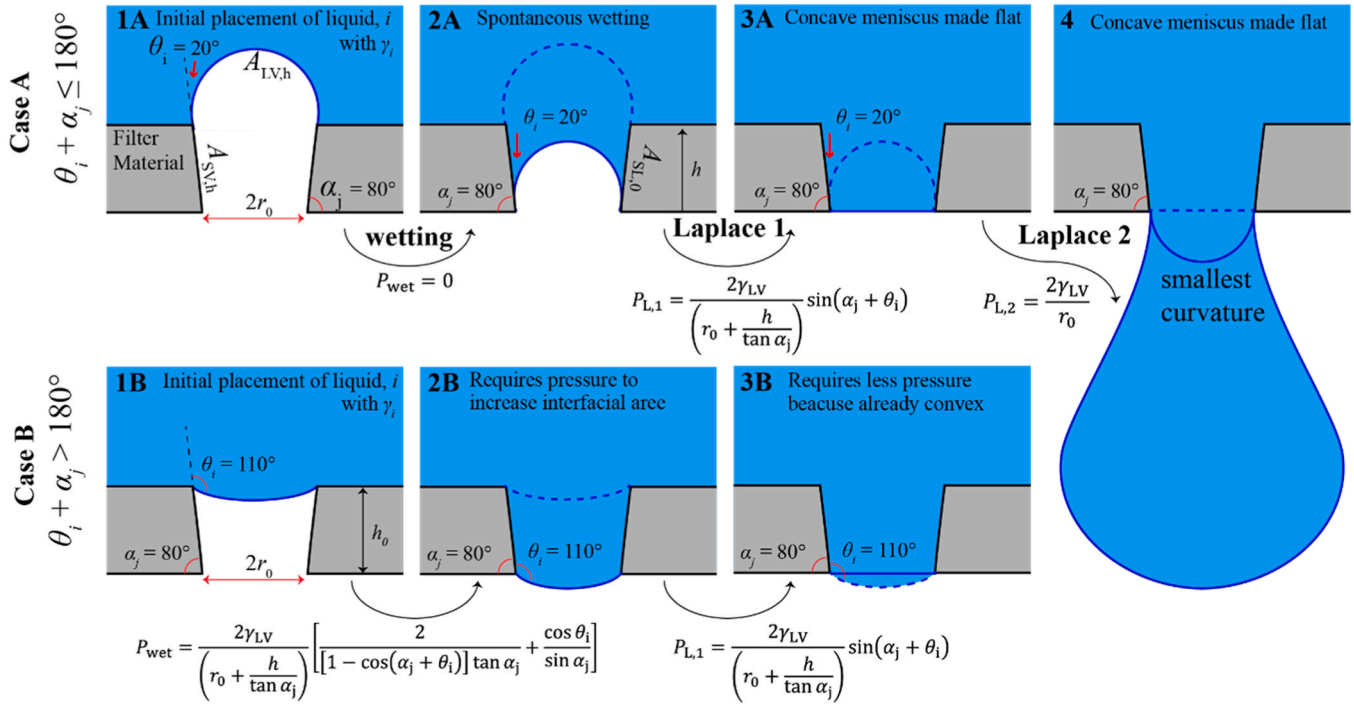

Fig. 3. States of permeation through a tapered cylindrical pore also showing the geometry and nomenclature used for the derivation.

$$A_{LV,h} = 2\pi\left(r_0 + \frac{h}{\tan\alpha_j}\right)^2 \frac{1}{1 - \cos(\alpha_j + \theta_i)}. \quad (5)$$

More details are given in Section 1 of Supporting Information. The area of the wall denoted as $A_{SL,0}$, which is the same as $A_{SV,h}$ is:

$$A_{SL,0} = A_{SV,h} = \pi(r_0 + r_{LV,h})s_{SV,h} = \frac{\pi h}{\sin\alpha_j}\left(2r_0 + \frac{h}{\tan\alpha_j}\right). \quad (6)$$

Substituting Eqs. (5) and (6) to Eq. (4) yields

$$E_2 - E_1 = \Delta E = -\pi h\gamma_{LV}\left(2r_0 + \frac{h}{\tan\alpha_j}\right)\left[\frac{2}{[1 - \cos(\alpha_j + \theta_i)]\tan\alpha_j} + \frac{\cos\theta_i}{\sin\alpha_j}\right] \quad (7)$$

Fig. 4 shows results for a sample calculation for water using pore dimensions similar to those in the experiments.

As Fig. 4 illustrates, $\Delta E > 0$ when $\alpha_j + \theta_i > 180°$ and $\Delta E < 0$ (spontaneous wetting) when $\alpha_j + \theta_i \leq 180°$. This observation aligns with the conclusions discussed by Kaufman et al. [40] Here we assume that the energy gained by the spontaneous wetting is dissipated by heat before it can be used to reshape the curvature of the vapor–liquid interface. Therefore, the energy at the bottom of the pore is reset to zero for Case A because the quantity of interest is the "extra" energy required for the transition from top to bottom. The demarcation between spontaneous and non-spontaneous wetting at $\alpha_j + \theta_i = 180°$ is our rationale for the two cases shown in Fig. 3. The force, $F(h)$, is:

$$F(h) = -\frac{dE}{dh} = 2\pi\gamma_{LV}\left(r_0 + \frac{h}{\tan\alpha_j}\right)\left[\frac{2}{[1 - \cos(\alpha_j + \theta_i)]\tan\alpha_j} + \frac{\cos\theta_i}{\sin\alpha_j}\right] \quad (8)$$

Since $\Delta E < 0$, i.e., $\alpha_j + \theta_i \leq 180°$, means a spontaneous transition from Panel 1 A to Panel 2 A, $F(h) > 0$ means a spontaneous transition. Therefore, $F(h)$ is understood as the force pulling the meniscus down. If it is negative, force is required to make the transition.

The pressure required to push the meniscus to each height is the force divided by the area of the pore at that height, $A(h)$. The positive value of $F(h)/A(h)$ represents the pressure pulling the meniscus down as with $F(h)$ because $A(h)$ is positive. However, the negative sign is added to $F(h)$ in describing the pressure needed to permeate because the pressure needed to overcome is of interest. To calculate this pressure that should be overcome to permeate, $P(h)$, the area of the pore at h should be calculated from the radius of the three-phase boundary at h given as $r(h) = r_0 + h/\tan\alpha_j$ (refer to Section 1 of the Supporting Information for further details). Therefore, dividing $\pi\, r(h)^2$ yields:

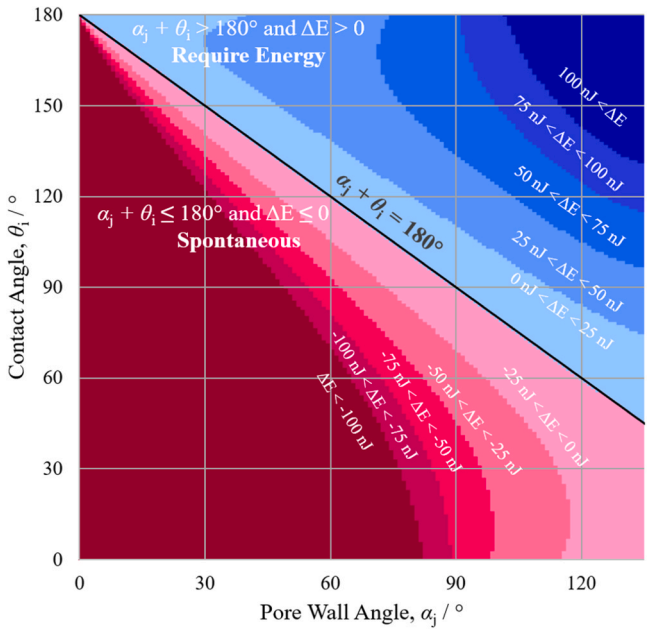

Fig. 4. Sample calculation of ΔE with Eq. (7) when γ_{LV} = 72 mN/m, r_0 = 0.4 mm, and h = 0.4 mm. With these values of r_0 and h, the radius at the top of the pore becomes negative at $\alpha_j > 135°$. Therefore, the data is present for $0 < \alpha_j < 135°$. ΔE values are expressed with different colors. Note that all energies are much greater in magnitude than kT. The red colors in different hues represent $\Delta E < 0$ and the blue colors represent $\Delta E > 0$. The diagonal black line represents the conditions where $\alpha_j + \theta_i = 180°$, at which the sign of ΔE changes.

$$P(h) = -\frac{2\gamma_{LV}}{\left(r_0 + \frac{h}{\tan\alpha_j}\right)}\left[\frac{2}{\left[1-\cos\left(\alpha_j+\theta_i\right)\right]\tan\alpha_j} + \frac{\cos\theta_i}{\sin\alpha_j}\right] \tag{9}$$

When this quantity is made positive, it represents the pressure that has to be overcome to transition from Panel 1–2.

For $\alpha_j \leq 90°$, it is important to note that the smallest area is always at the bottom of the pore ($h = 0$) making $r(h = 0) = r_0$. On the other hand, for $\alpha_j \leq 90°$, the top of the pore has the smallest area. Note that negative values of $r(h)$ are physically impossible. Therefore, Fig. 4 was prepared within the constraint that $r(h)$ is never negative. Within this limit of positive $r(h)$, the external pressure required to displace the meniscus from the top to the bottom of the pore, denoted as P_{wet}, can be described as follows:

$$P_{wet} = 0 \text{ if } \alpha_j + \theta_i \leq 180° \tag{10}$$

$$P_{wet} = -\frac{2\gamma_{LV}}{r_0}\left[\frac{2}{\left[1-\cos\left(\alpha_j+\theta_i\right)\right]\tan\alpha_j} + \frac{\cos\theta_i}{\sin\alpha_j}\right] \text{ if } \alpha_j + \theta_i > 180° \text{ and } \alpha_j \leq 90° \tag{11}$$

$$P_{wet} = -\frac{2\gamma_{LV}}{\left(r_0 + \frac{h}{\tan\alpha_j}\right)}\left[\frac{2}{\left[1-\cos\left(\alpha_j+\theta_i\right)\right]\tan\alpha_j} + \frac{\cos\theta_i}{\sin\alpha_j}\right] \text{ if } \alpha_j + \theta_i > 180° \text{ and } \alpha_j > 90° \tag{12}$$

The subsequent step involves flattening the meniscus by overcoming the Laplace pressure that maintains the meniscus in its concave (or convex) shape, as depicted in Panels 2 and 3 of Fig. 3. To calculate this pressure, it is necessary to determine the radius of curvature of the meniscus assuming it is a truncated sphere. The radius of curvature for a meniscus at a specific height, denoted as $R_{LV,h}$, can be obtained by referring to Section 1 of the Supporting Information. The pressure required to flatten the meniscus, $P_{L,1}$, can be calculated as follows:

$$P_{L,1} = \frac{2\gamma_{LV}}{r_0}\sin\left(\alpha_j + \theta_i\right) \text{ if } \alpha_j \leq 90° \tag{13}$$

$$P_{L,1} = \frac{2\gamma_{LV}}{\left(r_0 + \frac{h}{\tan\alpha_j}\right)}\sin\left(\alpha_j + \theta_i\right) \text{ if } \alpha_j > 90° \tag{14}$$

Note that there is no distinction between $\alpha_j + \theta_i > 180°$ or $\leq 180°$. Yet, the $P_{L,1}$ is negative when $\alpha_j + \theta_i > 180°$, thus requiring less total pressure to enable permeation.

The process continues with the flattened meniscus requiring further enlargement until the droplet becomes sufficiently large and heavy to detach from the bottom of the pore, as depicted in the transition from Panels 3–4. During this transition, the maximum required pressure occurs at the smallest radius of curvature, which occurs when the meniscus becomes a hemisphere with the radius r_0. For all larger pendant drops, the Laplace pressure is lower because the radius of curvature is lower. Providing the same hydrostatic head is maintained, the droplet will continue to increase in size until gravity drives detachment of the droplet. Regardless of any conditions posed by α_j and θ_i, the pressure needed to further make the meniscus grow, $P_{L,2}$, is;

$$P_{L,2} = \frac{2\gamma_{LV}}{r_0} \tag{15}$$

Therefore, the pressure needed for a liquid *i* that makes the contact angle with the filter material at θ_i, placed on the top of the tapered cylindrical pore at a certain angle α_j, symbolized by $P_{i,j}$, can be calculated as below in case of $\alpha_j > 90°$ by adding all three pressures, P_{wet}, $P_{L,1}$, and $P_{L,2}$.

$$P_{i,j} = \frac{2\gamma_{LV}}{\left(r_0 + \frac{h}{\tan\alpha_j}\right)}\left[\sin\left(\alpha_j+\theta_i\right) + 1 + \frac{h}{r_0\tan\alpha_j}\right] \text{ if } \alpha_j + \theta_i \leq 180° \tag{16}$$

$$P_{i,j} = \frac{2\gamma_{LV}}{\left(r_0 + \frac{h}{\tan\alpha_j}\right)}\left[-\frac{2}{\left[1-\cos\left(\alpha_j+\theta_i\right)\right]\tan\alpha_j} - \frac{\cos\theta_i}{\sin\alpha_j} + \sin\left(\alpha_j+\theta_i\right) + 1 + \frac{h}{r_0\tan\alpha_j}\right] \text{ if } \alpha_j + \theta_i > 180° \tag{17}$$

In the case of $\alpha_j \leq 90°$, the smallest area is at the bottom of the pore where $h = 0$. Substituting $h = 0$ to Eq. (16) and (17) yields;

$$P_{i,j} = \frac{2\gamma_{LV}}{r_0}\left[\sin\left(\alpha_j+\theta_i\right) + 1\right] \text{ if } \alpha_j + \theta_i \leq 180° \tag{18}$$

$$P_{i,j} = \frac{2\gamma_{LV}}{r_0}\left[-\frac{2}{\left[1-\cos\left(\alpha_j+\theta_i\right)\right]\tan\alpha_j} - \frac{\cos\theta_i}{\sin\alpha_j} + \sin\left(\alpha_j+\theta_i\right) + 1\right] \text{ if } \alpha_j + \theta_i > 180° \tag{19}$$

For experiments, the pressure was controlled by the height of water above the filter pore (the hydrostatic "head"), which is given as $H_{i,j} = P_{i,j}/\rho g$ with ρ being the density of the liquid and g the gravitational constant.

Though the equations were derived separately for the two cases, $\alpha_j \leq 90°$ and $\alpha_j > 90°$, they are eventually the same equation. For brevity, Eqs. (18) and (19) can be expressed as a dimensionless quantity by dividing the Laplace pressure for zero contact angle for the 90° pore, which is $2\gamma_{LV}/r_0$:

$$\frac{r_0 P_{i,j}}{2\gamma_{LV}} = \sin\left(\alpha_j+\theta_i\right) + 1 \text{ if } \alpha_j + \theta_i \leq 180° \tag{20}$$

$$\frac{r_0 P_{i,j}}{2\gamma_{LV}} = -\frac{2}{\left[1-\cos\left(\alpha_j+\theta_i\right)\right]\tan\alpha_j} - \frac{\cos\theta_i}{\sin\alpha_j} + \sin\left(\alpha_j+\theta_i\right) + 1 \text{ if } \alpha_j+\theta_i > 180^\circ \tag{21}$$

For example, the pressure required to permeate when $\alpha_j = 90^o$ and $\theta_i = 0$ is simply the pressure required to push the curvature from -r_0 to r_0, which is a pressure of 2 in dimensionless units

The experiments in this work are restricted to situations where $\alpha_j = 90^o$. For this condition, we have:

$$\frac{r_0 P_{i,j}}{2\gamma_{LV}} = \cos\theta_i + 1 \text{ if } \alpha_j+\theta_i \le 180^\circ \tag{22}$$

$$\frac{r_0 P_{i,j}}{2\gamma_{LV}} = 1 \text{ if } \alpha_j+\theta_i > 180^\circ \tag{23}$$

The dimensionless pressure to permeate as expressed with Eqs. (22) and (23) along with its three components at $\alpha_j = 90^o$ calculated using Eqs. (20) and (21), are shown in Fig. 5.

At this point, we remind readers that we assumed that the filling of the pore by liquid was done sufficiently slowly that the energy released between states 1 A and 2 A was lost before the energy was required for state 3 A. If the pore is filled quickly, some of this energy could conceivably be used to go further than state 2 A and in this case Eq. (20) provides an overestimate. Another important consideration is that the model system has sharp edges at the entrance and exit which is not physically realizable.

When considering the total pressure required, it may seem counter-intuitive that lower contact angles need more pressure. This is due to the pressure required to reverse the curvature of the meniscus at the pore exit. There are no contributions from P_{wet} when $\alpha_j + \theta_i \le 180^\circ$, and $P_{L,2}$ remains constant regardless of α_j and θ_i. At high θ_i which causes $\alpha_j + \theta_i > 180^\circ$, the convex meniscus requires negative Laplace pressure which offsets P_{wet} that increases with increasing θ_i. Since this criterion on having a constant value or changing values is determined by $\alpha_j + \theta_i$ and α_j is constant in this case, θ_i at which the trend changes is called the transition contact angle, or $\theta_{i,\,trans}$. With $\alpha_j = 90^\circ$, $\theta_i = 90^\circ$ as shown in Fig. 5.

The equations developed in this section were tested through experiments to investigate the impact of θ_i on $P_{i,j}$. To conduct these experiments, the height of water at which the first droplet detached from the filter materials was measured, with variations in the θ_i of water. This was done using the simplest geometry, with α_j set to 90°. The pores were prepared using a more realistic method, rather than employing a geometrically perfect setup that is challenging to achieve on an industrial scale, thus making the theory more practically applicable.

3. Experiments

3.1. Preparation of cylindrical pores

Pores of varying sizes were fabricated using 3D-printing based on 3D models, an example of which is depicted schematically in Fig. 6. The intended radius of these pores was 150, 200, and 250 micrometers, with a fixed height of 400 micrometers. To address issues related to the uncontrollable three-phase boundaries of the droplets forming at the bottom of the pore, a spout was added. The theory stipulated that the three-phase boundary should form at the bottom ridge of the pore as shown in Panel 4 of Fig. 3. To achieve this, a 50 μm thick spout was printed so that the three-phase boundary does not form randomly on a flat bottom surface. Furthermore, a weir was printed around the pore to attach a glass column, in which water was to be placed. The inner diameter of the weir's rim was 8.5 mm. These 3D-printed models are referred to as filters in the following discussion.

The 3D model was produced using a stereolithography (SLA) Form 2 printer, utilizing resin purchased from Formlabs Inc. This proprietary resin consisted of urethane dimethacrylate, methacrylate, and a photo initiator. The model was printed at a 45° angle compared to the major plane with a step size of 25 μm. Subsequently, the printed filters were immersed in isopropyl alcohol for 15 minutes to remove any excess resin. Dry air was used to blow through the pores and eliminate any remaining resin inside them. The filters were then post-cured for 30 minutes at 60°C. Once they reached room temperature, their pore radii were verified using an optical microscope. Additionally, a 3D laser profilometer (Zeta 20, Zeta Instruments) was employed to measure the pore radii and the surface roughness of the filters, both with and without

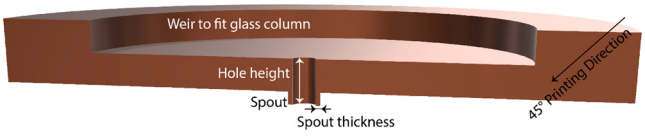

Fig. 6. Design of filters with a 90° pore with the names of different parts.

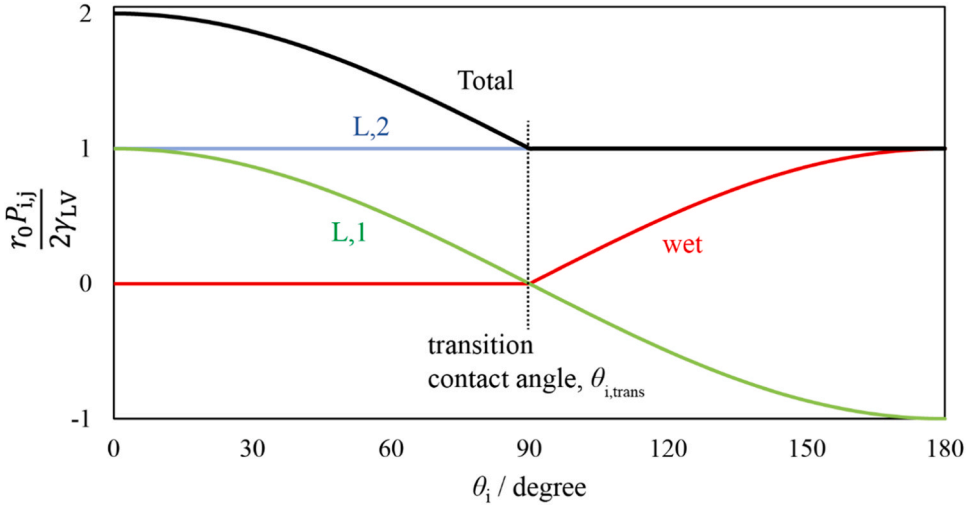

Fig. 5. Dimensionless pressure to permeate (solid black) as a function of contact angle with the contribution from each component. "wet" represents the pressure required to change the interfacial area, "L,1" for making the convex or concave meniscus flat by overcoming the Laplace pressure, and "L,2" for making the meniscus larger by overcoming the smallest radius at r_0, which is at the bottom of the pore. The transition contact angle is the angle at which the trend in dimensionless pressure shifts from increasing or decreasing to remaining constant.

a PDMS coating (further explained in the next paragraph). To minimize data deviation, it was decided to print a single pore per filter, as multiple pores had shown higher variability probably due to the limitation of 3D printers that produced differently-sized pores even with the same design.

To reduce roughness and facilitate control of the water contact angle on the filter, the filters were coated with polydimethylsiloxane (PDMS). Dow SYLGARD™ 184 Silicone Elastomer Clear (PDMS 184) was purchased and used as is. Several milliliters of a 10:1 mixture of PDMS and a curing agent were prepared and placed inside the circular weir. This mixture was then drawn through the bottom of the pore using a vacuum, ensuring that the wall of the pore and the bottom of the filter were coated. The vacuum was then applied from the top of the filter. This process was repeated multiple times to fully coat the pore's wall, remove excess PDMS, and prevent pore clogging. From the same batch of the mixture, a 3D-printed flat slab was also coated. This slab, named as the accompanying slab, was prepared because measuring the contact angle of water on the filter with the dimensions shown in Fig. 6 was challenging. Contact angle measurements were conducted on this accompanying slab. Both the filter and the accompanying slab were subsequently cured in an oven at 60°C for approximately 4 hours. After curing, the contact angle of water on the accompanying slab was measured.

3.2. Measurement of head to permeate

The filter, coated with PDMS and cured in an oven, was then affixed to a glass column by applying vacuum grease on the outside of the column and the topside of the weir. The assembled column was securely mounted vertically between two foam pieces to minimize the impact of external vibrations. A ruler was attached alongside the column for measurement purposes. Water was supplied to the column via a Teflon tube connected to a syringe pump. The end of the tube was positioned at the corner where the bottom of the column met the filter material to minimize flow-induced pressure fluctuations. Water was incrementally added, approximately one millimeter at a time, followed by a 2-minute wait period to reach equilibrium.

After each 1 mm addition of water, the glass column containing water was imaged to measure the height of the water meniscus inside the column. If the first droplet formed and left the spout during the 2-minute waiting period, the previous height was recorded as the head to permeate, denoted as $H_{i,j}$. Subsequently, the filter was detached from the glass column, and any grease on the outside of the weir was physically removed with a swab. The remaining grease was then cleaned with toluene and ethanol, followed by air drying. The accompanying slab underwent the same cleaning process and was subsequently attached to the glass column to repeat the measurement of $H_{i,j}$. This process was repeated at least four times to obtain at least four values of $H_{i,j}$ for a single contact angle.

After completing one set of experiments and cleaning the filter, both the filter and the accompanying slab were subjected to UV ozone treatment. An approximate time required to induce a certain degree of change in contact angles was known from a prior experiment conducted on a different piece of slab coated with the 10:1 ratio mixture of PDMS (refer to Section 2 of Supporting Information). Yet, accurate contact angle values were measured using the accompanying slab after each UV ozone treatment.

3.3. 3D fluorescent confocal microscopy

To visualize the 3D shapes of the meniscus in water saturated with fluorescein, a fluorescent confocal microscope (FV 1000, Olympus) was employed. Filters with single pores were prepared as previously described, with the exception that PDMS was dyed with Nile red before curing. The filters were oriented with their bottom sides facing the objective lens, which was mounted invertedly. Subsequently, water containing fluorescein was introduced into the weir, and the filter was covered with a microscope slide cover glass. The confocal microscope was configured to use a dual-channel excitation for a contrasted view of the PDMS coating and the deionized (DI) water with fluorescein inside the pores. To generate 3D images, *z*-axis scans were initiated just below the spout and continued throughout the entire height of the pore (400 μm) with a step height of 5 μm. Subsequently, ImageJ software was utilized to analyze the radius of curvature of the meniscus from the obtained images.

4. Results and discussion

4.1. Measured head to permeate

Fig. 7 shows the measured head to permeate as a function of the contact angle of water on filters for a cylindrical pore (α_j= 90°). As previously mentioned, these filters were coated with PDMS and then subjected to varying durations of UV ozone exposure to alter the contact angle. When compared to the calculated dimensionless pressure to permeate in Fig. 5, the experimental trend in Fig. 7 is the opposite. Fig. 5 shows a cosine-like decrease at the low θ_i, which transitions to a constant value when $\theta_i > 90°$. Yet, Fig. 7 shows a constant height to permeate at low θ_i, which transitions to a sine-like increase around 60 – 70° in θ_i. Consequently, alternative explanations are needed to explain the discrepancy. Given that $P_{L,2}$ remains constant irrespective of angles, the experimental changes with contact angle must be attributed to P_{wet} and/or $P_{L,1}$. Interestingly, the trend closely resembles that of P_{wet} alone, which raises questions about the presence of $P_{L,1}$. As a result, it is postulated that $P_{L,1}$ is negligible, and the transition contact angle, $\theta_{i,trans}$, is influenced by the geometric irregularities on the wall of the pore.

4.2. Formation of flat menisci regardless of contact angle

To test the hypothesis that $P_{L,1}$ is negligible, the shapes of menisci were imaged with a 3D fluorescent confocal microscope as shown in Fig. 8. Regardless of θ_i, the meniscus was flat while the meniscus for θ_i = 0° should be concave toward water (green) and θ_i = 130° be convex. To check both the resolution of the confocal and the effect of surface roughness, we measured the meniscus shape inside a smooth glass capillary. For the smooth glass capillary, a curved meniscus was resolved with the same microscope. (Refer to Section 3 of the Supporting Information for more detail.) Therefore, the flat meniscus was attributed to

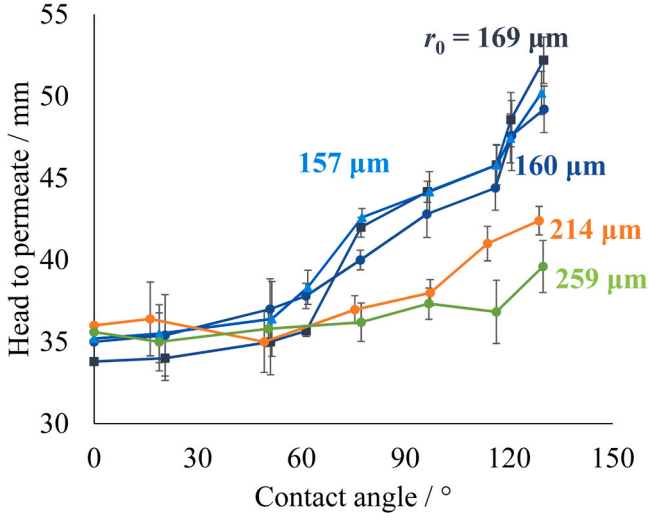

Fig. 7. Measured head to permeate as a function of contact angle of water through 3D-printed cylindrical pores. Dots are for data and the lines are guides to the eye. Values of r_0 are indicated on the graph.

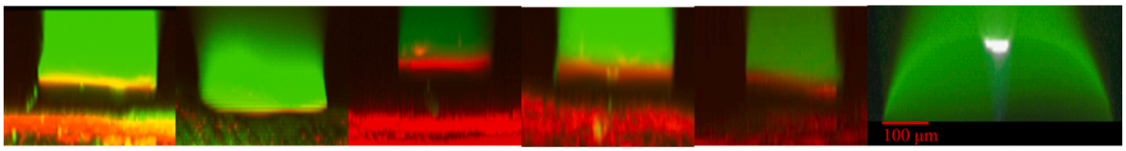

Fig. 8. Shapes of meniscus inside 3D-printed pores and coated with PDMS. Note that the green color is water saturated with fluorescein while the red is PDMS with Nile red. From left to right, the contact angles of water on PDMS were 0°, 60°, 76°, 118°, and 130°. The last image is the 3D-constructed meniscus of water dyed with fluorescein inside a smooth glass capillary with high water wettability.

the surface roughness of the pore. For this rough surface case, the meniscus is always flat and $P_{L,1}$ is negligible.

The formation of a flat meniscus is possible because of surface roughness. When the wall of the pore is not homogeneous in topography, there is not a unique relationship between θ_i, r_0, and the curvature of the liquid–vapor interface. The liquid can find a situation where the curvature is low, therefore the Laplace pressure is low. In the case of filters 3D-printed at a 45° angle, the printed pore would have a corrugated pore wall, as illustrated by the dotted line beneath the grey shading in Fig. 9. Although this wall was coated with PDMS to reduce roughness and create a smoother surface from the surface tension of PDMS before curing, it would still retain smoothed grooves. Consider a case where a liquid forms a contact angle of $\theta_i = 120°$ as depicted with the orange shade. This liquid can form a contact angle of $\theta_i = 120°$ with the filter material (grey shade) at some slope on the groove without creating a convex meniscus. Similarly, a liquid with $\theta_i = 40°$ (blue shade) can also form a flat meniscus even though the contact angle is non-zero. The availability of these low-curvature configurations means that the permeation can occur at a lower pressure.

Although not as pronounced as in Fig. 9, the 3D optical profilometry images of the pore's inner wall display angles on a scale of several micrometers to several tens of micrometers as illustrated in Fig. 10 and Figures S4 – S7 in Supporting Information. While the measurements in angle may not be highly precise due to a limited number of samples and noises due to the glossiness of PDMS surfaces, the angles can be between 13 – 20° considering the average and the standard deviation. This implies that α_j can vary between 70 and 110°.

As demonstrated in Fig. 4, an increase in α_j results in an increased ΔE, which in turn increases P_{wet}. Therefore, for the purpose of seeking the pressure above which permeation occurs, $\alpha_j = 107°$ (the average angle of 17° from five measurements added to the intended angle of 90°) was chosen when applying the modified theory discussed in the following section.

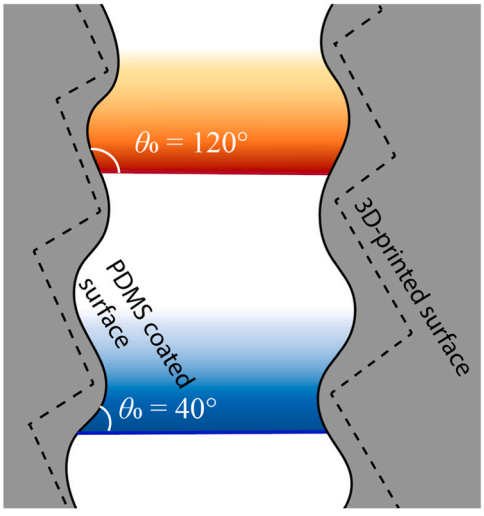

Fig. 9. Possible configuration of menisci from liquids with different contact angles. This depicts that flat menisci can form on grooved pore walls regardless of contact angle.

4.3. Modified theory

Eqs. (18) and (19) predict (as depicted in Fig. 5) the decrease of $P_{i,j}$ before $\alpha_j + \theta_i$ becomes greater than 180°, followed by a constant value when $\alpha_j + \theta_i > 180°$. Therefore, α_j can shift the $\theta_{i,trans}$ toward the smaller or larger θ_i. If assumed $\alpha_j = 90°$ as intended, $\theta_{i,trans} = 90°$ (see Fig. 5). However, the experimental trend in Fig. 7 showed $\theta_{i,trans}$ around 70 – 80°, which is a shift of 10 – 20°. This agrees with the approximate 13 – 20° change in slope discussed in the previous section.

We now assume that when the liquid exits the pore, it wets to the outer edge of the spout which has a wall thickness of 50 μm. This makes the exit radius $r_0 + 50$ μm. Eqs. (18) and (19) are modified to account for the increased exit radius, no effect from $P_{L,1}$, and divided by ρg to calculate the head. Therefore, $H_{i,j}$ is:

$$H_{i,j} = \frac{2\gamma_{LV}}{\rho g(r_0 + 50\mu m)} \text{ if } \alpha_j + \theta_i \le 180° \tag{24}$$

$$H_{i,j} = \frac{2\gamma_{LV}}{\rho g r_0}\left[-\frac{2}{[1-\cos(\alpha_j+\theta_i)]\tan\alpha_j} - \frac{\cos\theta_i}{\sin\alpha_j}\right] + \frac{2\gamma_{LV}}{\rho g(r_0+50\mu m)} \text{ if } \alpha_j + \theta_i > 180° \tag{25}$$

With $\gamma_{LV} = 72$ mN/m, $\rho = 1000$ kg/m^3, $g = 9.8$ m/s^2, and $r_0 = 150$, 200, 250 μm, the plot according to Eqs. (24) and (25) along with Fig. 7 (without showing the results from $r_0 = 157$ and 160 μm since they are similar to 159 μm) are shown in Fig. 11.

The trend from the experiments agrees well with the calculated trend, having larger $H_{i,j}$ as θ_i increases and the transition contact angle aligned with theory. Yet, two facts do not agree with the experiments. First, the value at the plateau at lower θ_i does not agree with the calculation. Second, the $H_{i,j}$ values from the calculation are about two to three times larger than the experimental value. Section 5 of Supporting Information discusses the possible explanation for the discrepancy, and the next section provides a brief summary.

4.4. Factors decreasing the pressure to permeate

The calculation is based on thermodynamic equilibrium, and does not consider other factors that may lower the pressure to permeate. These factors are discussed for more practical applications where they can be of importance.

First of all, the geometric uncertainty would play a role. As discussed, the 25-μm resolution limit from the 3D-printing provided grooves on the pore walls, and made the Laplace pressure much less. This resolution is comparable with the added radius of 50 μm to the pore size by printing the spout. This, or any defects from the printing, may form a pocket or dent that would help form droplets with unpredictable radii of curvature. Although spouts were meant to keep the positions of the three-phase boundary consistent, thus providing larger droplet size with larger r_0, the observation showed this trend was not always followed. (Refer to Section 5 of Supporting Information). This unexpected

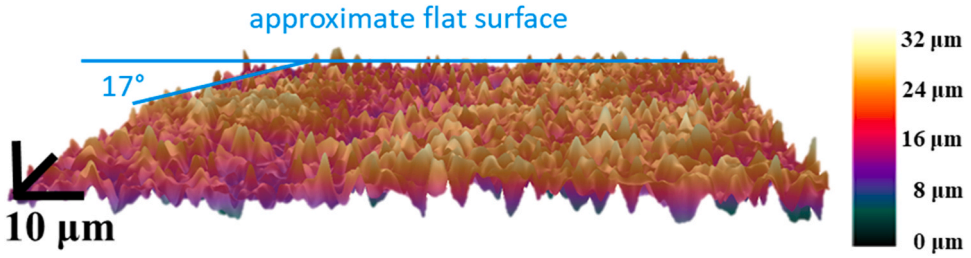

Fig. 10. 3D profilometry image of the wall of a pore. The approximate slopes at the bottom side of the profile were shown with light blue lines. Most small features (2 – 5 µm laterally) are noise due the glossiness of PDMS surfaces.

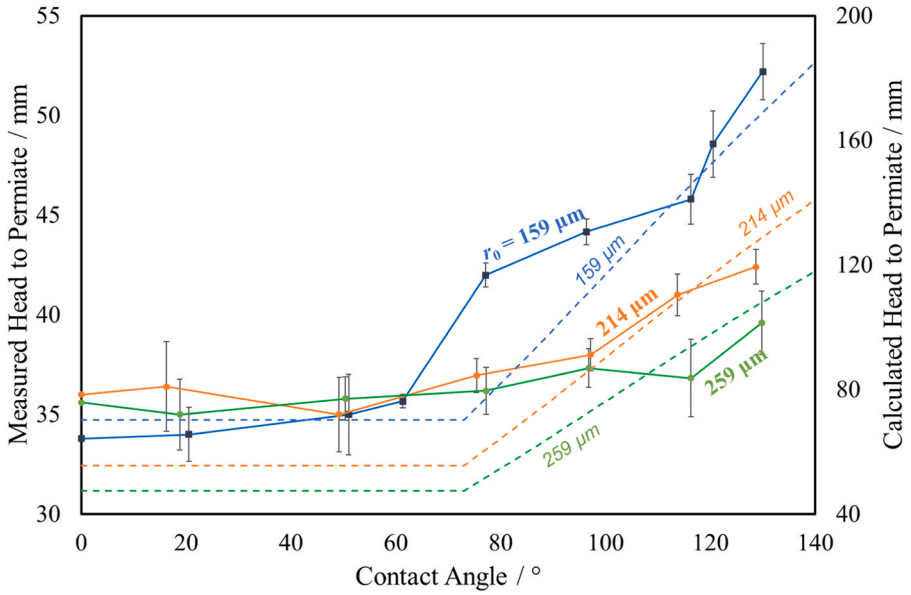

Fig. 11. Measured head to permeate (dots with straight lines, left axis) compared to calculated head to permeate (dotted lines, right axis) according to Eqs. (24) and (25). Blue lines are for the pore with r_0 = 159 µm, orange for 214 µm, and green for 259 µm.

variation would contribute to the discrepancy between the measurements and theory in predicting $P_{L,2}$.

Chemical inhomogeneity would also affect the pressure to permeate. As described in Eqs. (18) and (19) or Eqs. (24) and (25), θ_i controls the pressure to permeate. In case $\alpha_j + \theta_i \leq 180°$, water would spontaneously wet the pore wall and the meniscus would form at the bottom of the pore. If a part of the bottom area of the pore has impurities or defects that are more hydrophilic than the inside of the pore, water will wet the area spontaneously. As a consequence, the droplet can form in the more hydrophilic area, requiring less pressure to permeate.

The fluid flow may cause the pressure fluctuation that would be added to the hydrostatic head. Experiments were done in the same way presented in this paper except that the water was added continuously from a syringe pump. This design was discarded because it provided a very high deviation. These data can be found in Section 5 of Supporting Information, which showed lower heads to permeate compared to those reported in this article where the experiments were done by adding water incrementally. This confirms the effect of fluid flow in lowering the head to permeate. In addition, the fluid flow and pressure fluctuations may have contributed to the random advancement of the three-phase boundaries at the bottom toward the bottom surface of the spout.

5. Conclusions

We derived an equation that enables the calculation of the pressure required for a liquid to permeate through a tapered cylindrical pore. Of several variables in the equation, the effect of the contact angle of the liquid that permeates through the pore was tested experimentally in a practical setup where pores with radii varying from 150 to 250 µm were 3D-printed and coated with PDMS for easy control of the contact angle. The three steps of permeation were presented for the derivation of the pressure to permeate. The first step was for a liquid on the top of a pore to make more contact with the pore wall. This derivation closely followed that of Kaufman et al., [40] while the derivation in this paper can be applied more to general cases without geometric limitations. The second step was to calculate the Laplace pressure from the concave or convex shape of the liquid meniscus. The third step was about increasing the surface curvature until a liquid droplet would become heavy enough to leave the bottom of the filter. The pressures from these three steps were summed up to calculate the pressure to permeate. To verify the theory experimentally, filters with one pore were prepared, the contact angles were modified, water was added above the filter incrementally, and the hydraulic heads at which the first droplet left the pore were recorded as a function of the contact angle of water. Yet, the measured results showed an increase in the pressure to permeate with the increase in contact angles while the equation showed a decreasing trend. Thus, the theory was modified by hypothesizing that the Laplace pressure to be overcome from the second step was negligible. With this modification of the theory, the trend and the order of the measured and calculated values were reconciled. The Laplace pressure indeed was zero for any contact angles, verified with the flat shape of the meniscus at the liquid-vapor interface inside pores, which should be concave or convex depending on contact angles. This was attributed to the fact that the 3D-printed pore had roughness in which a flat meniscus could form

regardless of contact angles. Even after this correction, a discrepancy in the magnitude of the calculated and measured values remained. This is attributed to the effect of fluid flow that occurred when water was incrementally added, providing more pressure in addition to the hydraulic head.

This knowledge can be further utilized in the design and operation of filters for liquid-liquid separation by allowing the calculation of the threshold pressure for permeation with different liquids and geometries.

CRediT authorship contribution statement

Dongjin Seo: Writing – review & editing, Writing – original draft, Supervision, Project administration, Methodology, Funding acquisition, Formal analysis, Conceptualization. **Daniel Lippert:** Writing – original draft, Validation, Investigation, Formal analysis. **William Ducker:** Writing – review & editing, Investigation, Formal analysis.

Declaration of Competing Interest

The authors declare no competing interests.

Data availability

Data will be made available on request.

Acknowledgment

This research is funded by the National Science Foundation of the United States (CBET Award # 2012629).

Appendix A. Supporting information

Supplementary data associated with this article can be found in the online version at doi:10.1016/j.colsurfa.2024.133668.

References

[1] H. Kim, K. Noh, C. Choi, J. Khamwannah, D. Villwock, S. Jin, Extreme superomniphobicity of multiwalled 8 nm TiO2 nanotubes, Langmuir *27* (16) (2011) 10191–10196.
[2] T.C. France, F. Bot, A.L. Kelly, S.V. Crowley, J.A. O'Mahony, The influence of temperature on filtration performance and fouling during cold microfiltration of skim milk, Sep. Purif. Technol. *262* (2021) 118256.
[3] H.S. Abid, D.J. Johnson, R. Hashaikeh, N. Hilal, A review of efforts to reduce membrane fouling by control of feed spacer characteristics, Desalination *420* (2017) 384–402.
[4] W. Guo, H.-H. Ngo, J. Li, A mini-review on membrane fouling, Bioresour. Technol. *122* (2012) 27–34.
[5] D. Seo, J. Lee, C. Lee, Y. Nam, The effects of surface wettability on the fog and dew moisture harvesting performance on tubular surfaces, Sci. Rep. *6* (1) (2016) 1–11.
[6] D. Seo, A.M. Schrader, S.-Y. Chen, Y. Kaufman, T.R. Cristiani, S.H. Page, P. H. Koenig, Y. Gizaw, D.W. Lee, J.N. Israelachvili, Rates of cavity filling by liquids, Proc. Natl. Acad. Sci. (2018), https://doi.org/10.1073/pnas.1804437115.
[7] R.N. Wenzel, Resistance of solid surfaces to wetting by water, Ind. Eng. Chem. *28* (8) (1936) 988–994.
[8] A.B.D. Cassie, S. Baxter, Wettability of porous surfaces, 10.1039/TF9444000546, Trans. Faraday Soc. *40* (0) (1944) 546–551, https://doi.org/10.1039/TF9444000546.
[9] D. Bonn, Wetting transitions, Curr. Opin. Colloid *6* (1) (2001) 22–27, https://doi.org/10.1016/S1359-0294(00)00083-2.
[10] Israelachvili, J.N. *Intermolecular and surface forces*; Academic Press, 2011.
[11] T.M. Squires, S.R. Quake, Microfluidics: Fluid physics at the nanoliter scale, Rev. Mod. Phys. *77* (3) (2005) 977–1026, https://doi.org/10.1103/RevModPhys.77.977.
[12] S. Mukhopadhyay, S.S. Roy, R.A. D'Sa, A. Mathur, R.J. Holmes, J.A. McLaughlin, Nanoscale surface modifications to control capillary flow characteristics in PMMA microfluidic devices, Nanoscale Res. Lett. *6* (1) (2011) 411, https://doi.org/10.1186/1556-276X-6-411.
[13] R. Dangla, S.C. Kayi, C.N. Baroud, Droplet microfluidics driven by gradients of confinement, Proc. Natl. Acad. Sci. *110* (3) (2013) 853–858.
[14] Y. Wei, H. Qi, X. Gong, S. Zhao, Specially wettable membranes for oil–water separation, Adv. Mater. Interfaces *5* (23) (2018) 1800576, https://doi.org/10.1002/admi.201800576.
[15] M. Padaki, R.S. Murali, M.S. Abdullah, N. Misdan, A. Moslehyani, M. Kassim, N. Hilal, A. Ismail, Membrane technology enhancement in oil–water separation. A review, Desalination *357* (2015) 197–207.
[16] H.M. Mousa, H.S. Fahmy, G.A. Ali, H.N. Abdelhamid, M. Ateia, Membranes for oil/water separation: a review, Adv. Mater. Interfaces *9* (27) (2022) 2200557.
[17] A. Mansourizadeh, A. Javadi Azad, Preparation of blend polyethersulfone/cellulose acetate/polyethylene glycol asymmetric membranes for oil–water separation (journal article), J. Polym. Res. *21* (3) (2014) 375, https://doi.org/10.1007/s10965-014-0375-x.
[18] B. Chakrabarty, A.K. Ghoshal, M.K. Purkait, Ultrafiltration of stable oil-in-water emulsion by polysulfone membrane, J. Membr. Sci. *325* (1) (2008) 427–437, https://doi.org/10.1016/j.memsci.2008.08.007.
[19] B. Chakrabarty, A.K. Ghoshal, M.K. Purkait, Cross-flow ultrafiltration of stable oil-in-water emulsion using polysulfone membranes, Chem. Eng. J. *165* (2) (2010) 447–456, https://doi.org/10.1016/j.cej.2010.09.031.
[20] N.A. Ochoa, M. Masuelli, J. Marchese, Effect of hydrophilicity on fouling of an emulsified oil wastewater with PVDF/PMMA membranes, J. Membr. Sci. *226* (1) (2003) 203–211, https://doi.org/10.1016/j.memsci.2003.09.004.
[21] W. Chen, J. Peng, Y. Su, L. Zheng, L. Wang, Z. Jiang, Separation of oil/water emulsion using Pluronic F127 modified polyethersulfone ultrafiltration membranes, Sep. Purif. Technol. *66* (3) (2009) 591–597, https://doi.org/10.1016/j.seppur.2009.01.009.
[22] M. Joo, J. Shin, J. Kim, J.B. You, Y. Yoo, M.J. Kwak, M.S. Oh, S.G. Im, One-step synthesis of cross-linked ionic polymer thin films in vapor phase and its application to an oil/water separation membrane, J. Am. Chem. Soc. *139* (6) (2017) 2329–2337.
[23] B. Liang, G. Zhang, Z. Zhong, T. Sato, A. Hozumi, Z. Su, Substrate-independent polyzwitterionic coating for oil/water separation membranes, Chem. Eng. J. *362* (2019) 126–135.
[24] S. Bansal, V. von Arnim, T. Stegmaier, H. Planck, Effect of fibrous filter properties on the oil-in-water-emulsion separation and filtration performance, J. Hazard. Mater. *190* (1-3) (2011) 45–50.
[25] J. Zhang, W. Qu, X. Li, Z. Wang, Surface engineering of filter membranes with hydrogels for oil-in-water emulsion separation, Sep. Purif. Technol. *304* (2023) 122340, https://doi.org/10.1016/j.seppur.2022.122340.
[26] N.I. Abu-Lail, M. Kaholek, B. LaMattina, R.L. Clark, S. Zauscher, Micro-cantilevers with end-grafted stimulus-responsive polymer brushes for actuation and sensing, Sens. Actuators B: Chem. *114* (1) (2006) 371–378, https://doi.org/10.1016/j.snb.2005.06.003.
[27] M.A.C. Stuart, W.T.S. Huck, J. Genzer, M. Müller, C. Ober, M. Stamm, G. B. Sukhorukov, I. Szleifer, V.V. Tsukruk, M. Urban, F. Winnik, S. Zauscher, I. Luzinov, S. Minko, Emerging applications of stimuli-responsive polymer materials (Review Article), Nat. Mater. *9* (2010) 101, https://doi.org/10.1038/nmat2614.
[28] O. Azzaroni, A.A. Brown, W.T.S. Huck, UCST Wetting Transitions of Polyzwitterionic Brushes Driven by Self-Association, Angew. Chem. Int. Ed. *45* (11) (2006) 1770–1774, https://doi.org/10.1002/anie.200503264.
[29] D. Seo, W.A. Ducker, In Situ Control of Gas Flow by Modification of Gas-Solid Interactions, Phys. Rev. Lett. *111* (17) (2013) 174502, https://doi.org/10.1103/PhysRevLett.111.174502.
[30] R. Wang, J. Guo, G. Baran, S.L. Wunder, Characterization of the State of Order of Octadecylsilane Chains on Fumed Silica, Langmuir *16* (2) (2000) 568–576, https://doi.org/10.1021/la9908081.
[31] I. Tokarev, S. Minko, Multiresponsive, Hierarchically Structured Membranes: New, Challenging, Biomimetic Materials for Biosensors, Controlled Release, Biochemical Gates, and Nanoreactors, Adv. Mater. *21* (2) (2009) 241–247, https://doi.org/10.1002/adma.200801408.
[32] D. Lippert, J. Burnham, D. Seo, Active Control of Contact Angles of Various Liquids from the Response of Self-Assembled Thiol Molecules to Electric Current, Langmuir *39* (14) (2023) 5021–5030, https://doi.org/10.1021/acs.langmuir.3c00026.
[33] Seo, D.; Ducker, W.A. Control of Gas Flow in Narrow Channels Using an Electric Field To Modify the Flow Boundary Condition. *The Journal of Physical Chemistry C* 2014. DOI: 10.1021/jp500579b (acccessed 2014/04/07).
[34] N.L. Abbott, C.B. Gorman, G.M. Whitesides, Active Control of Wetting Using Applied Electrical Potentials and Self- Assembled Monolayers, Langmuir *11* (1) (1995) 16–18, https://doi.org/10.1021/la00001a005.
[35] A.W. Adamson, A.P. Gast, Physical chemistry of surfaces, Interscience, New York, 1967.
[36] F. Mugele, J.-C. Baret, Electrowetting: from basics to applications, J. Phys.: Condens. Matter *17* (28) (2005) R705.
[37] N. Liu, X. Lin, W. Zhang, Y. Cao, Y. Chen, L. Feng, Y. Wei, A Pure Inorganic ZnO-Co3O4 Overlapped Membrane for Efficient Oil/Water Emulsions Separation, Sci. Rep. -Uk *5* (1) (2015) 9688, https://doi.org/10.1038/srep09688.
[38] C.M. Gribble, G.P. Matthews, G.M. Laudone, A. Turner, C.J. Ridgway, J. Schoelkopf, P.A.C. Gane, Porometry, porosimetry, image analysis and void network modelling in the study of the pore-level properties of filters, Chem. Eng. Sci. *66* (16) (2011) 3701–3709, https://doi.org/10.1016/j.ces.2011.05.013.
[39] R.K. Gupta, G.J. Dunderdale, M.W. England, A. Hozumi, Oil/water separation techniques: a review of recent progresses and future directions, 10.1039/C7TA02070H, J. Mater. Chem. A *5* (31) (2017) 16025–16058, https://doi.org/10.1039/C7TA02070H.
[40] Y. Kaufman, S.-Y. Chen, H. Mishra, A.M. Schrader, D.W. Lee, S. Das, S. H. Donaldson, J.N. Israelachvili, Simple-to-Apply Wetting Model to Predict Thermodynamically Stable and Metastable Contact Angles on Textured/Rough/Patterned Surfaces, J. Phys. Chem. C. *121* (10) (2017) 5642–5656, https://doi.org/10.1021/acs.jpcc.7b00003.